Soft Matter

PAPER

View Article Online
View Journal

Cite this: DOI: 10.1039/d5sm00192g

Turbulent-like flows in quasi two-dimensional dense suspensions of motile colloids†

Rui Luo, [a] Alexey Snezhko [b] and Petia M. Vlahovska *[a]

Received 22nd February 2025,
Accepted 1st July 2025

DOI: 10.1039/d5sm00192g

rsc.li/soft-matter-journal

Dense bacterial suspensions exhibit turbulent-like flows at low Reynolds numbers, driven by the activity of the microswimmers. In this study, we develop a model system to examine these dynamics using motile colloids that mimic bacterial locomotion. The colloids are powered by the Quincke instability, which causes them to spontaneously roll in a random-walk pattern when exposed to a square-wave electric field. We experimentally investigate the flow dynamics in dense suspensions of these Quincke random walkers under quasi two-dimensional conditions, where the particle size is comparable to the gap between the electrodes. The results suggest a scaling regime in the energy spectrum $\sim k^{-4}$ at high wavenumbers, observed consistently across activity levels and particle concentrations. We observe that velocity time correlations decay within a single period of the square-wave field, yet an anti-correlation appears between successive field applications, indicative of a dynamic structural memory of the ensemble.

1 Introduction

Swimming bacteria self-organize into macroscopic patterns such as swarms and dynamic clusters.[1–7] At high concentrations, turbulent-like motion emerges characterized by erratic flows and transient vortices.[8–14] Unlike the classical hydrodynamic turbulence, which is a high-Reynolds number, inertia-dominated phenomenon, bacterial turbulence occurs at very low Reynolds numbers, where inertia is negligible, and is driven by the active motion of the microswimmers.[15] The energy spectrum in classical turbulence in two dimensions typically follows a power-law dependence on the wavenumber, $E \sim k^{-5/3}$, whereas for bacterial turbulence, different power laws have been reported.[10,16–18]

Active turbulence has been observed in various living fluids such as sperm,[20] microtubule-kinesin bundles (active nematics),[21–23] and cell tissues.[24,25] The phenomenon generated a lot of theoretical effort,[10,11,26–42] to decipher how "activity engenders turbulence".[43] Recently, a universal scaling of $E(k) \sim k^{-4}$ has been predicted and validated for two-dimensional active nematics systems,[44] and similar scaling has been observed in studies of bacterial turbulence transitioning from two-dimensional to three-dimensional flow, where such scaling is absent in purely two-dimensional conditions.[18] However, experimental research in bacterial turbulence lags behind the theoretical advances due to the challenges to have well defined and controllable conditions *e.g.*, particle density, speed (*i.e.*, activity) and locomotion type, when working with living microswimmers.

Synthetic externally driven colloids offer an alternative platform for studying active turbulence.[45–47] A promising model system to emulate bacterial flows is based on the Quincke rollers.[48–52] Their motility is due to an electrohydrodynamic instability, which gives rise to a constant electric torque on the particles[53] causing them to roll, if the particles are initially resting on the electrode. Quincke rollers exhibit a wide range of intricate collective behaviors.[48,54–58] Temporal modulation of the rollers' activity through application of a square-wave electric field modifies the rollers persistence length resulting in even richer collective dynamics.[19,59,60] By adjusting the durations of the pulses, τ_{on}, and their spacing, τ_{off}, the trajectory of an isolated Quincke roller becomes a random walk, and the particle locomotion can be tuned to emulate various bacterial motility patterns.[19] Populations of Quincke random walkers exhibit behaviors reminiscent of bacterial suspensions such as dynamic clustering in semi-dilute suspensions.[19]

Here, we employ dense suspensions of Quincke random walkers to gain insights into the turbulent-like flows of bacterial fluids. We consider suspensions confined between two parallel walls with spacing comparable to the colloid diameter, and experimentally measure spatial velocity correlations, structure functions, and kinetic energy spectra under varying concentrations of suspensions and activity, which is modulated by the applied field strength.

[a] Engineering Sciences and Applied Mathematics, Northwestern University, Evanston, IL 60208, USA. E-mail: petia.vlahovska@northwestern.edu
[b] Materials Science Division, Argonne National Laboratory, 9700 South Cass Avenue, Lemont, Illinois 60439, USA

† Electronic supplementary information (ESI) available. See DOI: https://doi.org/10.1039/d5sm00192g

2 Experiment

Spherical polymethyl methacrylate (PMMA) spheres (Phosphorex) with a diameter of d = 100 μm are dispersed in a 0.15 mol L^{-1} AOT-hexadecane solution (conductivity σ_f = 2.2 × 10^{-8} S m). The experimental chamber consists of two 7.5 × 5 cm^2 ITO-coated glass slides (Delta Technologies), separated by a ring-shaped Teflon tape with a thickness of 120 μm, see Fig. 1(a). The chamber is filled with the suspension solution. The particle motion and tracking is visualized using an inverted optical microscope (Zeiss) with 2× magnification mounted on a vibration isolation table (Kinetic Systems, Inc.). Videos were recorded at frame rates of 500 or 1000 frames per second by a high speed camera (Photron SA 1.1). The system is powered by a pre-designed pulsed electric field supplied by a high voltage amplifier (Matsusada) controlled by a function generator (Agilent Technologies 33521A). Particle tracking, flow field reconstruction and data analysis are carried out by means of particle image velocimetry (PIV) or particle tracking velocimetry (PTV) using open source Python codes (OpenPIV[61] and Trackpy[62]) as well as custom codes (see ESI† for details).

When a constant voltage is applied across the ITO electrodes, the particles become polarized due to the accumulation of free charges at their interfaces, generating an induced electric dipole oriented antiparallel to the applied electric field. Beyond a critical field strength, the dipole loses its symmetric orientation, triggering what is known as the Quincke electrorotation[63,64] and a particle rolls along the surface with a constant speed.[48,65] In our system, the typical threshold voltage for the onset of electrorotation is E_q = 1.6 V $μm^{-1}$ (Fig. 1(b)) and roller velocities ($\bar{v}$) range from 4 mm s^{-1} to 35 mm s^{-1}. The corresponding Reynolds number Re = $\rho_f \bar{v} d/2\mu_f$ ranges from 0.07 to 0.6, (here ρ_f = 0.77 g cm^{-3} and μ_f = 4.3 × 10^{-3} Pa s are the fluid density and viscosity, respectively). While typical Reynolds numbers in bacterial suspensions are significantly lower, the viscous forces are still dominant in this overdamped system.

When the electric field is pulsating, as shown in Fig. 1(c), the behavior of the roller changes. The roller "runs" while the field is on and stops when the field is turned off. Once the field is turned on again, the roller chooses a new random direction of rolling.[19] In a dense suspension, the resulting flow is illustrated in Fig. 1(d–f). Notably the external electric field imposes that all rollers stop and turn simultaneously unlike the stochastic tumbling of individual bacteria in dilute suspensions. Nevertheless, the globally synchronized run-stop behavior actually resembles dense bacterial suspensions where bacteria synchronize the tumbling due to mechanical

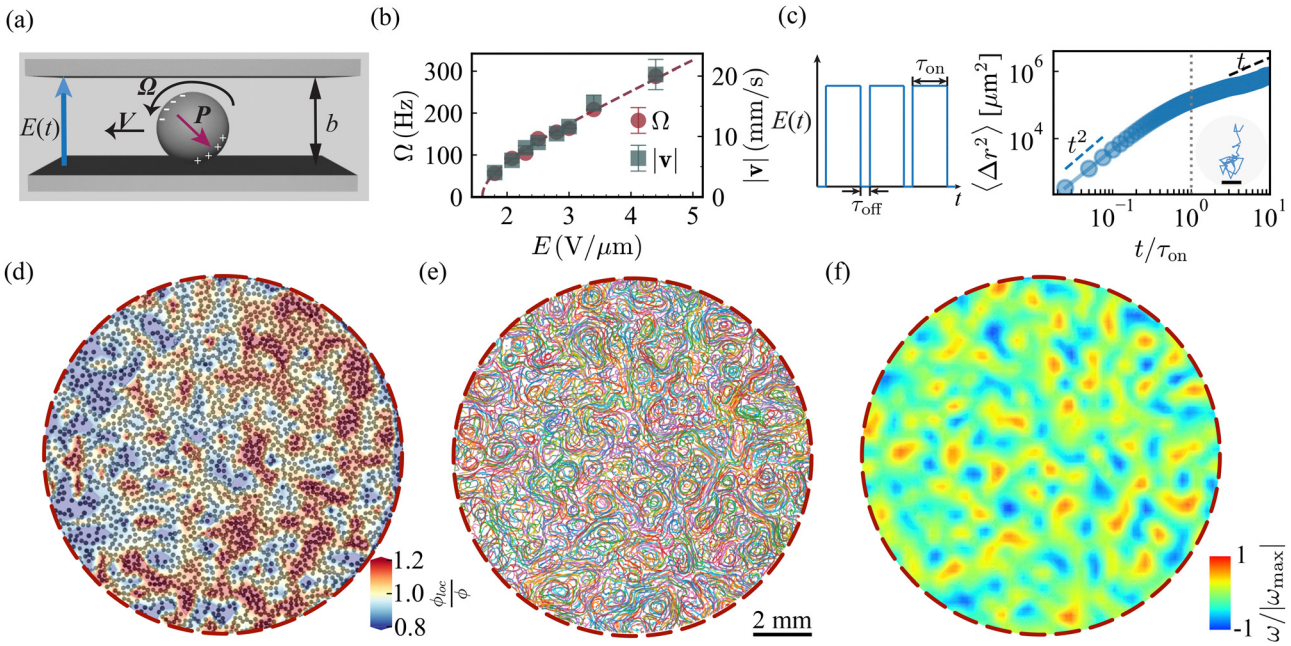

Fig. 1 Turbulent-like flows in suspension of Quincke random walkers: (a) in a uniform direct current (DC) electric field E, free charges accumulate at the particle surface. Above the threshold for the Quincke instability, the induced electric dipole tilts and generates a net torque, causing the sphere to roll in a randomly chosen direction in the plane perpendicular to the applied field direction. (b) The rotation rate as well as the rolling speed, *i.e.*, activity, of an individual Quincke roller increases with field strength. (c) Temporal modulation of the electric field in the form of a square-wave causes the particle to undergo a random walk[19] (see ESI,† Movie S1), if τ_{off} is much longer than the "particle memory" time τ_{MW} (the time required for complete depolarization). The mean-squared displacement ($\langle \Delta r^2 \rangle$) of a single Quincke random walker is shown for E = 4.4 V mm^{-1}, τ_{on} = 40 ms, and τ_{off} = 20 ms, with the corresponding trajectory displayed in the inset. Scale bar: 1 mm. (d) Snapshot of the colloidal suspension (area fraction ϕ = 0.51) overlaid with the local density map (background color). Vortices (panel f) nucleate preferentially in high-density regions. (e) Particle trajectories, tracked using particle tracking velocimetry (PTV), during one period τ_{on}. (f) Vorticity computed based on the velocity field from particle imaging velocimetry (PIV). The red dashed line indicates the field of view, not a physical boundary. The experiment is conducted at E = 7.4 V $μm^{-1}$, particle area fraction ϕ = 0.51. See ESI,† Movie S2. Movie S3 (ESI†) illustrates the flow for lower field strength and lower particle fraction (E = 2.8 V $μm^{-1}$,ϕ = 0.27).

locking of flagella.[66,67] This suggests that, although the microscopic triggering mechanisms differ (electric field *vs.* flagellar switching), the resulting active turbulent-like flow is robust to the specific details of the random walk, in particular the probability distribution of the run times. In our experiments, we vary the field magnitude E while maintaining fixed pulse durations τ_{on} = 40 ms and intervals τ_{off} = 20 ms. The off-time is chosen to be much longer than the Maxwell–Wagner polarization relaxation time $t_{MW} = (\varepsilon_p + 2\varepsilon_f)/(\sigma_p + 2\sigma_f) \approx 2$ ms, to ensure that the roller executes an uncorrelated random walk. $\varepsilon_{p,f}$ and $\sigma_{p,f}$ are the permittivities and conductivities of the particle (p) and the suspending fluid (f), respectively. The experimental values used are $\varepsilon_p = 3.2 \times 10^{-11}$ F m^{-1}, $\varepsilon_f = 1.77 \times 10^{-11}$ F m^{-1}; $\sigma_p = 1.0 \times 10^{-17}$ S m, $\sigma_f = 2.2 \times 10^{-8}$ S m. τ_{on} sets the particle persistence length and it is chosen so that it is comparable to the collision time, which varies from 7 ms to 38 ms. The average collision time of the particles is estimated based on the average particle number density, $\tau_{col} = \frac{1}{nd\langle|\mathbf{v}|\rangle}$, where n is the number density of particles, d is the particle's diameter, and $\langle|\mathbf{v}|\rangle$ is the average speed of the particles. The suspension is confined within a chamber bound by a ring-shaped Teflon tape (inner diameter 2.2 cm). To maintain the same gap between the electrodes in all experiments, we first fill the chamber with pure AOT-hexadecane solution before introducing approximately 40 mL of particle suspension at the chamber center. This protocol prevents particles from entering the space between the tape and the electrodes, which could disrupt electrode alignment. It establishes a central region of uniform particle density (1.6 cm diameter) surrounded by an outer region where the particle concentration decreases toward the chamber boundary. Over experimental timescales, we observe particle migration toward the boundary, though concentration variations in the field of view remain limited to less than 5% during measurement periods.

3 Results

3.1 Flow structure

A unique feature of the Quincke random walkers is that when the field is on, they all run, and when the field is turned off, they all stop, see Fig. 2(a). At lower activity and particle fraction, $E = 1.7E_q$, $\phi = 0.27$, the flow driven by the colloids reaches a steady state within one cycle while the field is on. However, higher activity and particle numbers, $E = 4.6E_q$, $\phi = 0.66$, give rise to a more vigorous flow, which does not reach the steady state within the period of the applied electric field. The distinct flow development patterns observed in Fig. 2(a) arise primarily from particle inertia effects at elevated field strengths. For $E = 7.4$ V mm^{-1}, rotation frequencies $\Omega \approx 500$ Hz as estimated from single roller measurement (Fig. 1(b)), yielding a rotational Reynolds number $\mathrm{Re}_\Omega = \rho_f(2\pi\Omega)d^2/(4\mu_f) \approx 1.4$. This non-negligible inertia results in longer times to reach a steady velocity.[65,68] Fig. 2(b) shows the velocity distribution for the experiments with low activity, low density ($E = 1.7E_q$, $\phi = 0.2$)

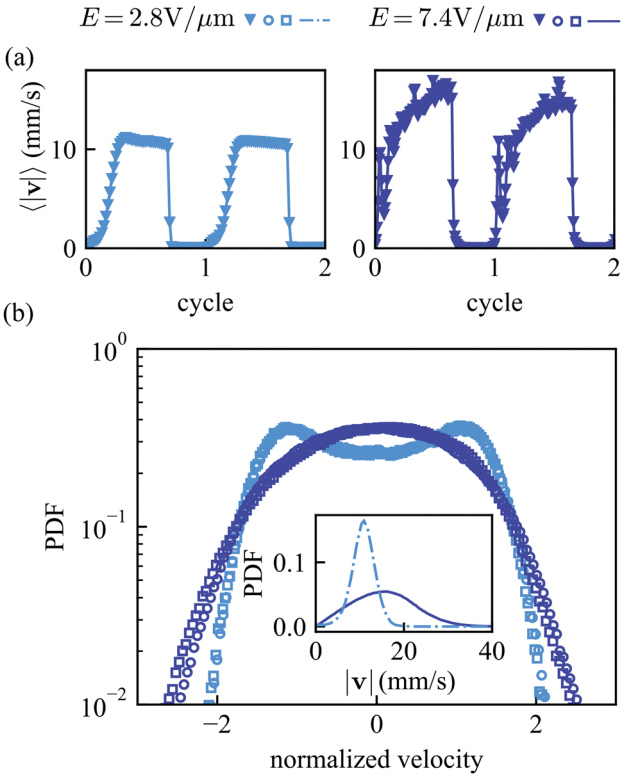

Fig. 2 (a) Mean particle flow velocity as a function of time during electric field pulsations. At low field strength (left, $E = 1.7E_q$, $\phi = 0.2$), particles reach a steady state quickly, while at high field strength (right, $E = 4.6E_q$, $\phi = 0.6$), particles take longer to reach a steady state. (b) Velocity distribution at $E = 1.7E_q$, $\phi = 0.2$ (blue) and $E = 4.6E_q$, $\phi = 0.6$ (purple). Circles denote the x-component of velocity, while squares denote the y-component. Inset: corresponding probability distribution function of the velocity magnitudes ($|\mathbf{v}|$).

and higher activity, high density ($E = 4.6E_q$, $\phi = 0.6$) systems. A bimodal structure of the PDF suggests that the particles are running with similar velocities; the sampling of the random velocity directions results in two peaks.[69] At higher concentrations, the probability density function (PDF) approaches a Gaussian distribution with a single peak. This occurs because particles now experience multiple collisions within the same time interval between two consecutive frames, t_{fps}, used to determine their velocities ($\tau_{col} < t_{fps}$).

To characterize the flow structure, we compute the velocity spatial correlation function

$$C_s(R) = \frac{\langle \mathbf{v}(r) \cdot \mathbf{v}(r+R)\rangle_r}{\langle \mathbf{v}^2(r)\rangle_r} \quad (1)$$

where $\mathbf{v}$ is the field velocity, and $\langle\cdot\rangle_r$ is the spatial average over all positions r. The velocity field is obtained directly from particle image velocimetry (PIV) for experiments with dense suspensions $\phi > 0.5$ or by interpolation based on individual particle velocity results from particle tracking velocimetry (PTV) for experiments with low particle density $\phi < 0.4$. The velocity correlation function $C_s(r)$ demonstrates characteristic anticorrelations (negative values of $C_s(r)$) that reveal the presence of a vortical motion in the system (Fig. 3(a)). Such anticorrelations

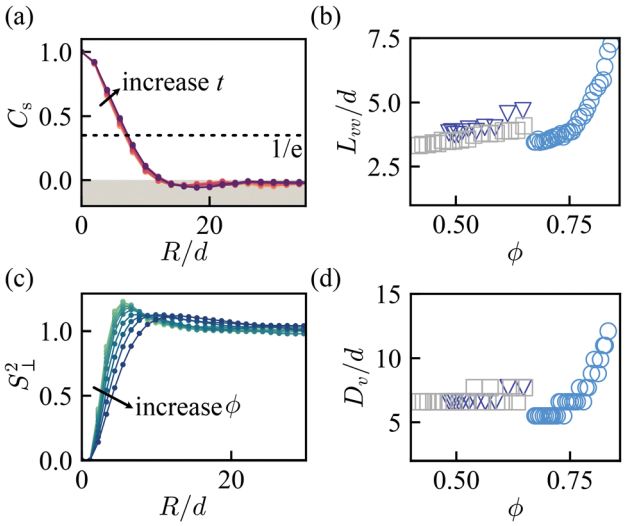

Fig. 3 (a) Velocity spatial correlation function ($C_s(R)$) within one period. $E = 1.7E_q$, $\phi = 0.84$. The correlation length (L_{vv}) is defined at the location where $C_s(R) = 1/e$. (b) Velocity correlation length L_{vv} as a function of concentration (ϕ) at different field strengths (circle: $E = 1.7E_q$; square: $E = 2.8E_q$; triangle: $E = 4.6E_q$). (c) Angular-averaged normalized two-point velocity correlation function *vs.* normalized radial distance at $E = 1.7E_q$ with increasing ϕ from 0.67 to 0.85. The peak position of $S_\perp{}^2$ indicates the effective vortex diameter D_v. (d) The effective vortex diameter increases with ϕ.

arise because particles on opposite sides of a vortex core move in antiparallel directions—a signature of rotational flow. While a single system-spanning vortex can produce perfect anticorrelations ($C_s = -1$),[48,70] the superposition of multiple vortices with distributed sizes leads to a shallower minimum as their contributions average out. The position of the minimum provides information about the average vortex size, while its depth reflects the degree of rotational order in the system. The characteristic velocity correlation length, L_{vv}, defined from the decay of the velocity correlation function ($C_s(L_{vv}) = 1/e$), quantifies the spatial coherence of collective motion. As shown in Fig. 3(b), L_{vv} increases with the particle fraction as reduced interparticle spacing strengthens hydrodynamic and electrostatic coupling. This growth reflects the formation of larger coherent structures, ultimately leading to system-spanning vortical patterns at high activity levels.

The transverse velocity structure function $S_\perp{}^2(R)$ provides insight into vortex statistics.[10,18] Defined as:

$$S_\perp{}^2(R) = \frac{\left\langle [(\mathbf{v}(\mathbf{r}+\mathbf{R}) - \mathbf{v}(\mathbf{r}))\cdot \mathbf{e}_\perp]^2 \right\rangle}{\langle \mathbf{v}^2(\mathbf{r})\rangle} \quad (2)$$

where $\mathbf{v}(\mathbf{r}+\mathbf{R}) - \mathbf{v}(\mathbf{r})$ is the velocity increment and $\mathbf{e}_\perp$ is a direction orthogonal to $\mathbf{R}$, this quantity specifically probes rotational motion by considering only velocity components perpendicular to the separation vector $\mathbf{R}$. The maximum in $S_\perp{}^2(R)$ corresponds to the characteristic vortex size, reflecting maximal velocity differences due to rotational flow. Fig. 3(c) shows the transverse velocity structure function $S_\perp{}^2(R)$ at $E = 1.6E_q$ for varying area fractions ϕ. The peak location, corresponding to the mean vortex size D_v, systematically shifts to larger R with increasing density. As shown in Fig. 3(d), this growth of D_v with ϕ follows the same trend as the velocity correlation length L_{vv}, demonstrating how enhanced hydrodynamic, and likely electrostatic as well, coupling at higher particle concentrations leads to extended ranges of velocity correlations and larger coherent structures. The parallel scaling of these two quantities highlights how local energy injection becomes organized into increasingly large-scale flow patterns as the system density increases.[71]

The vortex size distribution can be further investigated using the Okubo–Weiss (OW) parameter.[32,44] The OW parameter is defined as

$$\mathrm{OW} = (\partial_x v_x + \partial_y v_y)^2 - 4(\partial_x v_x)(\partial_y v_y) + 4(\partial_x v_y)(\partial_y v_x). \quad (3)$$

Regions with OW < 0 correspond to vortex regions. To analyze the vortex size distribution, we compute the histogram of the areas of connected vortex regions. This distribution, denoted as $n(a) = N(a)/\sum_a N(a)$, represents the normalized frequency of vortices with area a, where $N(a)$ is the number of vortices of area a. We find that $n(a)$ follows an exponential distribution, $n(a) \propto \exp(-a/a^*)$, where a^* is the mean vortex area and $D_{\mathrm{OW}} = 2\sqrt{a^*/\pi}$ is the mean vortex diameter. In Fig. 4 we demonstrate the vortex size distribution for two experimental conditions reported in the text. Their fitted dimensionless mean vortex diameters (D_{OW}/d) are 4.3 and 6.1, where d is the particle diameter. These values are comparable to the mean vortex diameter extracted from the perpendicular structure function in Fig. 3(d).

3.2 Kinetic energy spectrum

We next examine how the kinetic energy E is distributed across different length scales for varying field strengths and particle concentrations. The energy spectrum, *i.e.*, the energy of a vortex with size $\sim 1/k$, $E(k)$ is computed from the velocity field $\mathbf{v}(\mathbf{r},t)$ through the relation[10,44,72–74]

$$E(k) = \frac{k}{4\pi L^2}\langle |\hat{\mathbf{v}}(\mathbf{k})|^2 \rangle \quad (4)$$

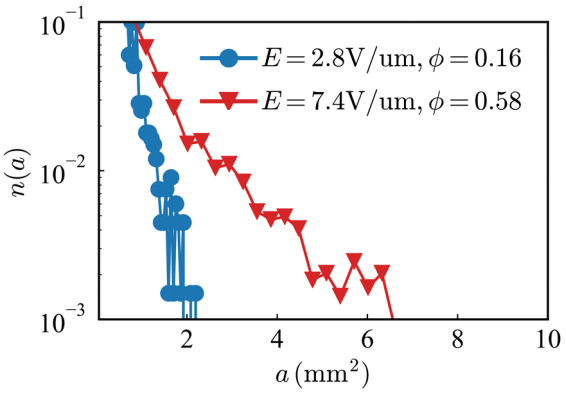

Fig. 4 Vortex size distributions from two representative experiments (OW analysis), exhibiting exponential decay.

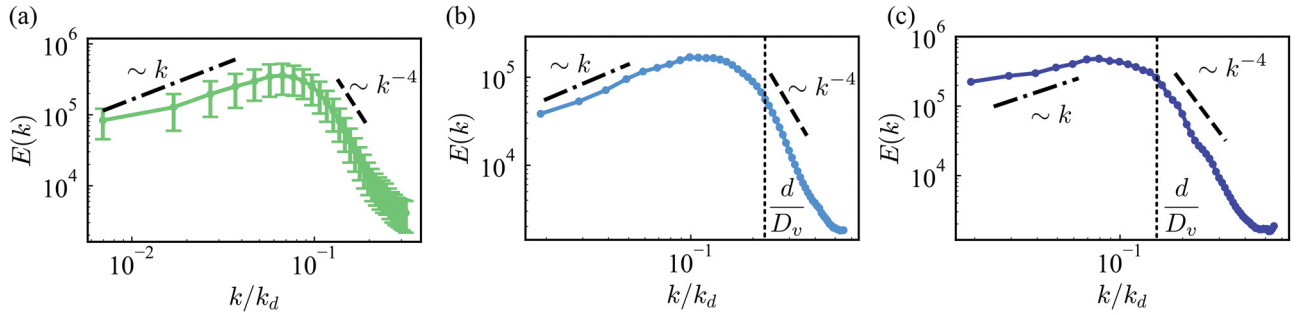

Fig. 5 (a) The kinetic energy spectrum exhibits similar behavior across varied concentrations and field strengths. $E(k) \sim k$ at small k and $E(k) \sim k^{-4}$ at large k. The experiment is performed at $E = 1.7E_q$, $\phi = 0.07$. (b) The energy spectra at $E = 1.7E_q$, $\phi = 0.16$, and (c) $E = 4.6E_q$, $\phi = 0.58$ exhibit the k^{-4} scaling for $k > 1/D_v$.

where $k = |\mathbf{k}|$ is the wavenumber, L^2 is the system area and $\hat{\mathbf{v}}(\mathbf{k}) = \int_{\mathbb{R}^2} \mathbf{v}(\mathbf{r}) e^{-i\mathbf{k}\cdot\mathbf{r}} d\mathbf{r}$ is the Fourier transformation of velocity. $E = L^2 \int_0^\infty E(k) dk$ is the total energy per unit mass of the system.

Fig. 5 shows the energy spectra for our system, revealing two distinct scaling regimes that characterize the flow properties at different length scales across all experimental conditions. The spectrum exhibits a linear dependence $E(k) \sim k$ at small wavenumbers ($k \ll 1/D_v$) indicating uncorrelated flow. This behavior can be understood through the Wiener–Khinchin relation, $E(k) = \frac{\pi}{A} k \left\langle \int C_s(\mathbf{R}) e^{-i\mathbf{k}\cdot\mathbf{R}} d\mathbf{R} \right\rangle_\theta$ where $C_s(\mathbf{R})$ is the spatial velocity correlation function and $\langle\cdot\rangle_\theta$ denotes averaging over the azimuthal angle θ. The linear scaling indicates that the velocity correlations become negligible on length scales longer than D_v, causing the Fourier transform of the velocity correlation function to approach a constant at small k.

Notably, at larger wavenumbers ($k > 1/D_v$), we find $E(k) \sim k^{-4}$ scaling, similar to observations in confined bacterial suspensions and 2D active nematics.[18,32,44] The crossover between regimes occurs near $k \approx 1/D_v$ (Fig. 5(b and c)), where D_v is the average vortex size. The exponential vortex size distribution and k^{-4} scaling in the vortex-dominated regime appear across different confined active systems, suggesting common statistical properties of active turbulence under confinement.

3.3 Temporal memory effects

It was recently demonstrated[60] that Quincke rollers in a globally correlated collective state (vortex) spontaneously develop structural positional ordering that "imprints" the chiral state of the system. Under a cessation and restoration of the activity facilitated by a pulsed field with both τ_{on} and τ_{off} significantly larger than all relevant timescales, a global vortex alternates its chiral state with each activity cycle. This periodic response, despite the absence of memory at the level of individual particles, was attributed to a phenomenon referred to as collective or "structural memory".[60] To investigate whether a similar "memory" phenomenon occurs in our system under a pulsating field with shorter τ_{on}, we compute the temporal correlation function of the velocity field,

$$C_{T,vf}(\tau) = N^{-1} \sum_i \langle \mathbf{v}_i(t) \cdot \mathbf{v}_i(t+\tau) \rangle_t \Big/ \langle \mathbf{v}_i^2(t) \rangle_t \qquad (5)$$

and the vorticity field,

$$C_{T,\omega}(\tau) = N^{-1} \sum_i \langle \omega_i(t) \cdot \omega_i(t+\tau) \rangle_t \Big/ \langle \omega_i^2(t) \rangle_t \qquad (6)$$

Here, the system is divided into a square grid. $\mathbf{v}_i$ is the average velocity at the cell i; N is the total number of cells and $\langle\cdot\rangle_t$ denotes the time average. Similarly, we compute the vorticity field ω_i based on the velocity field and proceed to compute the vorticity temporal correlation function.

Within one cycle, see Fig. 6(a), the time correlation function decays to zero, indicating that at a fixed location, the flow field decorrelates from its initial state, likely due to the particle collisions. Nevertheless, when the time correlation function is computed between the pulses (stroboscopically- at fixed time within each period), the correlation functions exhibit clear non-negligible anti-correlations after one cycle (see Fig. 6(b)) indicative of the velocity and vorticity reversals in the ensemble during temporal activity cycling. This finding indicates that at the subsequent cycle, a vortex is likely to occur at the same location but with opposite direction of rotation. This behavior is attributed to structural memory, facilitated by local particle positional asymmetries in self-organized roller vortices.[60] In our system under short activity pulses, local vortices do not coalesce into a giant vortex. Nonetheless, the formation of these locally correlated vortical states is the source of the anti-correlations in the system between the activity cycles. Only particles participating in local vortices contribute to the anti-correlations resulting in a correlation value significantly lower than -1 (as it is with a global vortex state[60]). The signature of the collective ensemble memory is robust and easily detectable. Over time (beyond 2 cycles) the correlations between the activity cycles are suppressed as the locations of vortices get randomized. The anti-correlation exhibits a non-monotonic dependence on particle concentration as structural memory gets suppressed with increased concentration, similarly to ref. 60 (see ESI† for details).

4 Conclusion

We have investigated active turbulence in a system of Quincke random walkers, a synthetic system which mimics the run-and-tumble behavior of bacteria. The Quincke random walkers

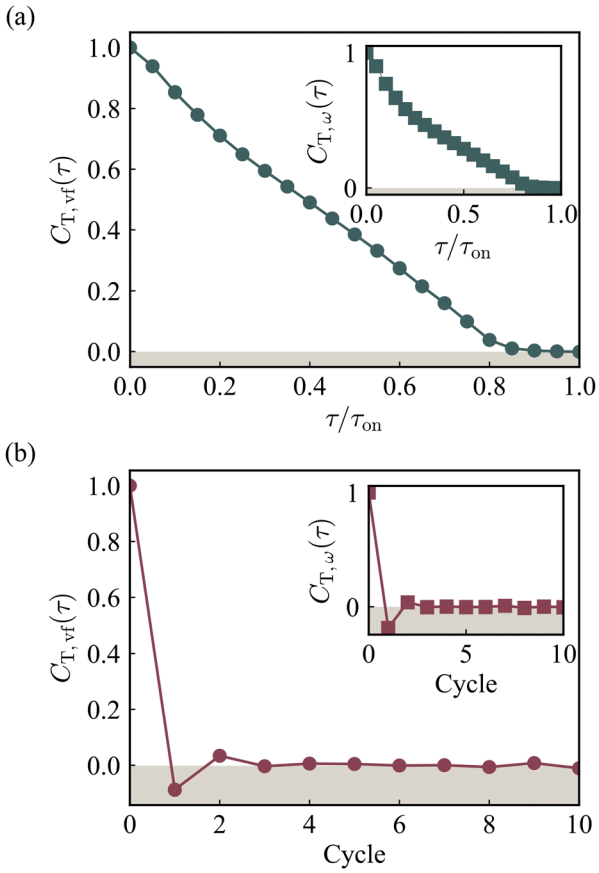

Fig. 6 Temporal correlations of the velocity and vorticity fields (E = 1.7E_q, ϕ = 0.74). (a) Within a single field cycle, the velocity field (and vorticity field shown in the inset) decorrelates over time. (b) Stroboscopic temporal correlations of velocity field (inset: vorticity field) exhibit anti-correlation between subsequent field pulses.

provide a versatile experimental model of active matter to study the fundamental mechanisms of active turbulence. We observe that the kinetic energy spectra follow k^{-4} scaling, consistent with the observations in very confined bacterial suspensions.[18] Our experiments indicate exponential vortex size distribution, which has been previously observed in active nematic turbulence and bacterial turbulence. In addition, the quasi-two-dimensional dense suspension of random walkers undergoing synchronized run-and-tumble behavior showed evidence of structural collective memory. Our findings highlight the importance of transient dynamic memory in the ensemble, both at the particle level and collective, in accessing unconventional self-organized states.

Author contributions

PV and AS conceived the research. RL designed and carried out the experiments and analyzed the data. All authors discussed the results and wrote the paper.

Conflicts of interest

There are no conflicts to declare.

Data availability

Data for this article, including movies will be available at Research and Data Repository at **https://arch.library.northwestern.edu**.

Acknowledgements

The research of R. L. and P. V. was supported by NSF-DMR award 2004926. The research of A. S. was supported by the U.S. Department of Energy, Office of Science, Basic Energy Sciences, Materials Sciences and Engineering Division.

References

1 M. F. Copeland and D. B. Weibel, *Soft Matter*, 2009, **5**, 1174–1187.
2 H. Zhang, A. Be'Er, R. S. Smith, E.-L. Florin and H. L. Swinney, *Europhys. Lett.*, 2009, **87**, 48011.
3 H. P. Zhang, A. Be'er, E.-L. Florin and H. L. Swinney, *Proc. Natl. Acad. Sci. U. S. A.*, 2010, **107**, 13626–13630.
4 X. Chen, X. Dong, A. Be'er, H. L. Swinney and H. Zhang, *Phys. Rev. Lett.*, 2012, **108**, 148101.
5 X. Chen, X. Yang, M. Yang and H. Zhang, *Europhys. Lett.*, 2015, **111**, 54002.
6 A. Be'er, B. Ilkanaiv, R. Gross, D. B. Kearns, S. Heidenreich, M. Baer and G. Ariel, *Commun. Phys.*, 2020, **3**, 66.
7 I. S. Aranson, *Rep. Prog. Phys.*, 2022, **85**, 076601.
8 C. Dombrowski, L. Cisneros, S. Chatkaew, R. Goldstein and J. Kessler, *Phys. Rev. Lett.*, 2004, **93**, 098103.
9 A. Sokolov, I. S. Aranson, J. O. Kessler and R. E. Goldstein, *Phys. Rev. Lett.*, 2007, **98**, 158102.
10 H. H. Wensink, J. Dunkel, S. Heidenreich, K. Drescher, R. E. Goldstein, H. Löwen and J. M. Yeomans, *Proc. Natl. Acad. Sci. U. S. A.*, 2012, **109**, 14308–14313.
11 J. Dunkel, S. Heidenreich, K. Drescher, H. H. Wensink, M. Bär and R. E. Goldstein, *Phys. Rev. Lett.*, 2013, **110**, 228102.
12 J. Gachelin, A. Rousselet, A. Lindner and E. Clement, *New J. Phys.*, 2014, **16**, 025003.
13 S. Zhou, A. Sokolov, O. D. Lavrentovich and I. S. Aranson, *Proc. Natl. Acad. Sci. U. S. A.*, 2014, **111**, 1265–1270.
14 Y. Peng, Z. Liu and X. Cheng, *Sci. Adv.*, 2021, **7**, eabd1240.
15 R. Alert, J. Casademunt and J.-F. Joanny, *Annu. Rev. Fluid Mech.*, 2022, **13**, 143–170.
16 D. Saintillan and M. J. Shelley, *J. R. Soc. Interface*, 2012, **9**, 571–585.
17 Z. Liu, W. Zeng, X. Ma and X. Cheng, *Soft Matter*, 2021, **17**, 10806–10817.
18 D. Wei, Y. Yang, X. Wei, R. Golestanian, M. Li, F. Meng and Y. Peng, *Adv. Sci.*, 2024, 2402643.
19 H. Karani, G. E. Pradillo and P. M. Vlahovska, *Phys. Rev. Lett.*, 2019, **123**, 208002.
20 A. Creppy, O. Praud, X. Druart, P. L. Kohnke and F. Plourabou¥'e, *Phys. Rev. E: Stat., Nonlinear, Soft Matter Phys.*, 2015, **92**, 032722.

21 T. Sanchez, D. N. Chen, S. DeCamp, M. Heymann and Z. Dogic, *Nature*, 2012, **491**, 431.
22 A. Opathalage, M. M. Norton, M. P. N. Juniper, B. Langeslay, S. A. Aghvami, S. Fraden and Z. Dogic, *Proc. Natl. Acad. Sci. U. S. A.*, 2019, **116**, 4788–4797.
23 B. Martinez-Prat, J. Ignes-Mullol, J. Casademunt and F. Sagues, *Nat. Phys.*, 2019, **15**, 362.
24 C. Blanch-Mercader, V. Yashunsky, S. Garcia, G. Duclos, L. Giomi and P. Silberzan, *Phys. Rev. Lett.*, 2018, **120**, 208101.
25 S.-Z. Lin, W.-Y. Zhang, D. Bi, B. Li and X.-Q. Feng, *Commun. Phys.*, 2021, **4**, 21.
26 R. Aditi Simha and S. Ramaswamy, *Phys. Rev. Lett.*, 2002, **89**, 058101.
27 D. Saintillan and M. Shelley, *Phys. Rev. Lett.*, 2007, **99**, 058102.
28 D. Saintillan and M. J. Shelley, *J. R. Soc. Interface*, 2012, **9**, 571–585.
29 D. Saintillan and M. J. Shelley, *C. R. Phys.*, 2013, **14**, 497–517.
30 J. Dunkel, S. Heidenreich, M. Br and R. E. Goldstein, *New J. Phys.*, 2013, **15**, 045016.
31 V. Bratanov, F. Jenko and E. Frey, *Proc. Natl. Acad. Sci. U. S. A.*, 2015, **112**, 15048–15053.
32 L. Giomi, *Phys. Rev. X*, 2015, **5**, 031003.
33 M. James, W. J. T. Bos and M. Wilczek, *Phys. Rev. Fluids*, 2018, **3**, 061101.
34 A. Doostmohammadi, J. Ignes-Mullol, J. M. Yeomans and F. Sagues, *Nat. Commun.*, 2018, **9**, 3246.
35 M. Linkmann, G. Boffetta, M. C. Marchetti and B. Eckhardt, *Phys. Rev. Lett.*, 2019, **122**, 214503.
36 V. S. Škultéty, C. Nardini, J. Stenhammar, D. Marenduzzo and A. Morozov, *Phys. Rev. X*, 2020, **10**, 031059.
37 M. R. Shaebani, A. Wysocki, R. G. Winkler, G. Gompper and H. Rieger, *Nat. Rev. Phys.*, 2020, **2**, 181–199.
38 K. Qi, E. Westphal, G. Gompper and R. G. Winkler, *Commun. Phys.*, 2022, **5**, 1–12.
39 A. W. Zantop and H. Stark, *Soft Matter*, 2022, **18**, 6179–6191.
40 Y.-E. Keta, J. U. Klamser, R. L. Jack and L. Berthier, *Phys. Rev. Lett.*, 2024, **132**, 218301.
41 Q. Yang, M. Jiang, F. Picano and L. Zhu, *Nat. Commun.*, 2024, **15**, 2874.
42 S. Goh, E. Westphal, R. G. Winkler and G. Gompper, *Phys. Rev. Res.*, 2025, **7**, 013142.
43 S. Fraden, *Nat. Phys.*, 2019, **15**, 311–312.
44 B. Martínez-Prat, R. Alert, F. Meng, J. Ignés-Mullol, J.-F. Joanny, J. Casademunt, R. Golestanian and F. Sagués, *Phys. Rev. X*, 2021, **11**, 031065.
45 D. Nishiguchi and M. Sano, *Phys. Rev. E: Stat., Nonlinear, Soft Matter Phys.*, 2015, **92**, 052309.
46 G. Kokot, S. Das, R. G. Winkler, G. Gompper, I. S. Aranson and A. Snezhko, *Proc. Natl. Acad. Sci. U. S. A.*, 2017, **114**, 12870–12875.
47 J. Mecke, Y. Gao, C. A. Ramrez Medina, D. G. Aarts, G. Gompper and M. Ripoll, *Commun. Phys.*, 2023, **6**, 324.
48 A. Bricard, J.-B. Caussin, N. Desreumaux, O. Dauchot and D. Bartolo, *Nature*, 2013, **503**, 95–98.
49 M. Driscoll and B. Delmotte, *Curr. Opin. Colloid Interface Sci.*, 2019, **40**, 42–57.
50 A. Boymelgreen, J. Schiffbauer, B. Khusid and G. Yossifon, *Curr. Opin. Colloid Interface Sci.*, 2022, 101603.
51 N. M. Diwakar, G. Kunti, T. Miloh, G. Yossifon and O. D. Velev, *Curr. Opin. Colloid Interface Sci.*, 2022, 101586.
52 K. J. Bishop, S. L. Biswal and B. Bharti, *Annu. Rev. Chem. Biomol. Eng.*, 2023, **14**, 1–30.
53 G. Quincke, *Ann. Phys.*, 1896, **295**, 417–486.
54 A. Bricard, J.-B. Caussin, D. Das, C. Savoie, V. Chikkadi, K. Shitara, O. Chepizhko, F. Peruani, D. Saintillan and D. Bartolo, *Nat. Commun.*, 2015, **6**, 7470.
55 A. Chardac, S. Shankar, M. C. Marchetti and D. Bartolo, *Proc. Natl. Acad. Sci. U. S. A.*, 2021, **118**, e2018218118.
56 B. Zhang, A. Sokolov and A. Snezhko, *Nat. Commun.*, 2020, **11**, 4401.
57 B. Zhang, A. Snezhko and A. Sokolov, *Phys. Rev. Lett.*, 2022, **128**, 018004.
58 C. Jorge, A. Chardac, A. Poncet and D. Bartolo, *Nat. Phys.*, 2024, **20**, 303–309.
59 B. Zhang, H. Karani, P. M. Vlahovska and A. Snezhko, *Soft Matter*, 2021, **17**, 4818–4825.
60 B. Zhang, H. Yuan, A. Sokolov, M. O. De La Cruz and A. Snezhko, *Nat. Phys.*, 2022, **18**, 154–159.
61 A. Liberzon, T. Käufer, A. Bauer, P. Vennemann and E. Zimmer, *OpenPIV/Openpiv-Python: OpenPIV-python v0.23.4, Zenodo*, 2021.
62 D. B. Allan, T. Caswell, N. C. Keim, C. M. van der Wel and R. W. Verweij, *Soft-Matter/Trackpy: V0.6.4, Zenodo*, 2024.
63 E. Lemaire and L. Lobry, *Physica A*, 2002, **314**, 663–671.
64 T. B. Jones, *IEEE Trans. Ind. Appl.*, 1984, **20**, 845–849.
65 G. E. Pradillo, H. Karani and P. M. Vlahovska, *Soft Matter*, 2019, **15**, 6564–6570.
66 H. P. Zhang, A. Be'er, E.-L. Florin and H. L. Swinney, *Proc. Natl. Acad. Sci. U. S. A.*, 2010, **107**, 13626–13630.
67 M. F. Copeland and D. B. Weibel, *Soft Matter*, 2009, **5**, 1174–1187.
68 Y. Wang, S. Canic, G. Kokot, A. Snezhko and I. S. Aranson, *Phys. Rev. Fluids*, 2019, **4**, 013701.
69 G. Kokot, A. Vilfan, A. Glatz and A. Snezhko, *Soft Matter*, 2019, **15**, 3612–3619.
70 B. Zhang, H. Yuan, A. Sokolov, M. O. De La Cruz and A. Snezhko, *Nat. Phys.*, 2022, **18**, 154–159.
71 J. Mecke, Y. Gao, G. Gompper and M. Ripoll, *Commun. Phys.*, 2024, **7**, 1–10.
72 R. H. Kraichnan and D. Montgomery, *Rep. Prog. Phys.*, 1980, **43**, 547.
73 G. Boffetta and R. E. Ecke, *Annu. Rev. Fluid Mech.*, 2012, (44), 427–451.
74 U. Frisch, *Turbulence: The Legacy of A. N. Kolmogorov*, Cambridge University Press, 1995.